

Biomimetic Design of Mitochondria-Targeted Hybrid Nanozymes as Superoxide Scavengers

Yue Zhang, Anila Khalique, Xinchun Du, Zhanxia Gao, Jin Wu, Xiangyun Zhang, Ran Zhang, Zhiyuan Sun, Qiqi Liu, Zhelong Xu, Adam C. Midgley, Lianyong Wang, Xiyun Yan, Jie Zhuang,* Deling Kong,* and Xinglu Huang*

Development of enzyme mimics for the scavenging of excessive mitochondrial superoxide ($O_2^{\cdot-}$) can serve as an effective strategy in the treatment of many diseases. Here, protein reconstruction technology and nanotechnology is taken advantage of to biomimetically create an artificial hybrid nanozyme. These nanozymes consist of ferritin-heavy-chain-based protein as the enzyme scaffold and a metal nanoparticle core as the enzyme active center. This artificial cascade nanozyme possesses superoxide dismutase- and catalase-like activities and also targets mitochondria by overcoming multiple biological barriers. Using cardiac ischemia-reperfusion animal models, the protective advantages of the hybrid nanozymes are demonstrated in vivo during mitochondrial oxidative injury and in the recovery of heart functionality following infarction via systemic delivery and localized release from adhesive hydrogels (i.e., cardiac patch), respectively. This study illustrates a de novo design strategy in the development of enzyme mimics and provides a promising therapeutic option for alleviating oxidative damage in regenerative medicine.

Excessive reactive oxygen species (ROS), especially superoxide radicals ($O_2^{\cdot-}$), play critical roles in the pathogenesis of many diseases, including ischemia-reperfusion (IR) injury.^[1] The mechanisms of IR injury are complicated and not fully understood, but a well-characterized initiating factor is the burst of $O_2^{\cdot-}$ ROS from the mitochondrial respiratory chain upon reperfusion.^[2,3] Thus, protecting mitochondria from $O_2^{\cdot-}$ -induced damage is essential for the development of new approaches to alleviate IR injury. Superoxide dismutases (SOD) are the primary antioxidant defense system in the body, which catalyze

$O_2^{\cdot-}$ into oxygen and H_2O_2 . In mammals, SOD are composed of three subtypes with different subcellular localization, including cytoplasmic Cu/Zn SOD, mitochondrial Mn SOD, and extracellular Cu/Zn SOD.^[2] The development of therapeutics aimed at delivering SOD to target tissues has brought the potential of treating various dysfunctions.^[4] However, the main drawbacks of using native SOD in therapy include the expenses incurred to produce the protein, easily inactivated enzymatic activity, poor membrane permeability, and nonspecific targeting,^[5] which greatly limit the potential applications of native SOD delivery in the alleviation of IR injury.

As a new type of promising artificial enzyme, nanozymes have been shown to possess advantages over natural enzymes, such as low cost, high stability and durability, and multifunctionality.^[6,7] Nanozymes are capable of producing and/or scavenging cytotoxic free radicals by mimicking natural enzyme activities, such as peroxidase (POD),^[8] SOD,^[9] and catalase (CAT) activities.^[10] As such, creation of nanozymes for scavenging cytotoxic free radicals has recently exhibited promising prospects within regenerative medicine.^[7] However, utilization of nanozymes to remove $O_2^{\cdot-}$ from mitochondria via SOD-like activity is challenging due to intrinsic limitations of nanozymes. First, almost all synthetic nanozymes possess POD-like activity, despite rarely being shown in many reports. POD

Dr. Y. Zhang, A. Khalique, X. Du, Z. Gao, J. Wu, X. Zhang, Dr. R. Zhang, Dr. Z. Sun, Q. Liu, Prof. A. C. Midgley, Prof. L. Wang, Prof. X. Yan, Prof. J. Zhuang, Prof. D. Kong, Prof. X. Huang
Key Laboratory of Bioactive Materials for the Ministry of Education
College of Life Sciences
State Key Laboratory of Medicinal Chemical Biology
Nankai University
Tianjin 300071, China
E-mail: zhuangj@nankai.edu.cn; kongdeling@nankai.edu.cn;
huangxinglu@nankai.edu.cn

Dr. Y. Zhang, Prof. Z. Xu
Department of Physiology and Pathophysiology
Tianjin Medical University
Tianjin 300070, China

Z. Gao, Prof. J. Zhuang
School of Medicine
Nankai University
Tianjin 300071, China

J. Wu, Prof. X. Yan, Prof. J. Zhuang, Prof. X. Huang
Joint Laboratory of Nanozymes
College of Life Sciences
Nankai University
Tianjin 300071, China

Prof. X. Yan
CAS Engineering Laboratory for Nanozymes
Institute of Biophysics
Chinese Academy of Sciences
Beijing 100101, China

 The ORCID identification number(s) for the author(s) of this article can be found under <https://doi.org/10.1002/adma.202006570>.

DOI: 10.1002/adma.202006570

activity decomposes H_2O_2 to produce highly cytotoxic hydroxyl free radicals (OH^\cdot). Second, the nanozymes with SOD-like activity that catalyze $\text{O}_2^{\cdot-}$ into H_2O_2 increase the risk of further conversion to OH^\cdot . Thus, an ideal nanozyme for $\text{O}_2^{\cdot-}$ removal should be capable of not only catalyzing $\text{O}_2^{\cdot-}$ into nontoxic molecules but also preventing additional OH^\cdot production.

Learning from nature, we hypothesized that mimicking Mn SOD activity could address the above issue since Mn SOD is mainly responsible for scavenging $\text{O}_2^{\cdot-}$ in mitochondrial oxidative stress to maintain intracellular homeostasis.^[11] As a native metalloenzyme, the metal active site and protein scaffold of SOD determine enzymatic activity.^[12] In this study, we conceptually created an artificial hybrid enzyme based on a de novo design strategy: we integrated in situ synthesis of Mn-based nanoparticles with human-protein derived nanocages obtained by recombinant gene and protein expression. Moreover, we endowed the nanozyme with mitochondria-targeting abilities and the capability to overcome the intracellular lysosome barrier, via triphenylphosphonium (TPP)-based modification.^[13] As a model, we chose mouse cardiac IR injury for in vivo therapeutic assessment potential of the mitochondria-targeted cascade nanozymes delivered by intravenous (i.v.) injection or by local release from transplanted cardiac patches made from tissue-adhesive hydrogel.

De novo design and synthesis of native enzyme mimetics is a challenge for synthetic biology. A key factor in the development of an enzyme mimic is the selection of a suitable protein scaffold that can house active centers. Recombinant human ferritin nanocage (FTn) consists of 24 ferritin heavy chain subunits, which fold to form a symmetrical structure of six C_4 channels and eight C_3 channels.^[14] The C_3 channels allow the entry of hydrophilic metal ions from solution into the inner cavity of FTn. The ferroxidase site, composed of three amino acid residues (Glu27, His65, Glu62), actively binds metal ions,^[15] providing the location for metal ion nucleation into the particles. Thus, we chose FTn as an ideal protein scaffold for the design of nanozymes. The preparation of the mitochondria-targeted hybrid nanozymes is shown in the scheme of **Figure 1a**. In a typical procedure, recombinant ferritin nanocages (FTn) were synthesized by genetic overexpression in *E. coli* using a custom-made plasmid encoding human native ferritin heavy chain, followed by production and purification of the FTn protein. The resulting FTn showed a cage-like structure composed of the assembly of 24 ferritin heavy chain subunits. Next, the in situ incorporation of MnO_2 particles into the FTn cavity was performed by taking advantage of the existing intrinsic properties of FTn for the capture and nucleation of Mn^{2+} ^[16] (**Figure S1a**, Supporting Information). Next, a lipophilic cation, TPP, was introduced and conjugated onto the FTn surface to enable mitochondria targeting, owing to charge attraction to the negative membrane potential of mitochondria.^[17] Transmission electron microscopy (TEM) revealed the uniform diameter of the hollow structure of FTn was ≈ 12 nm after protein negative staining (**Figure 1b**). The diameter of FTn inner cavity is 8 nm, and the incorporated MnO_2 nanozymes within the FTn core (MnO_2 Fenozymes) were observed by TEM. The MnO_2 Fenozymes showed monodispersed spherical morphology (**Figure 1c**) with mean diameters of ≈ 6.5 nm, which did not change after TPP conjugation (**Figure 1d**). The zeta potential changes from -2.3

to $+21.8$ mV revealed successful TPP conjugation onto the MnO_2 Fenozymes (**Figure S1b**, Supporting Information).

We sought to test whether MnO_2 Fenozymes possessed enzyme-like activity by using the substrates for natural enzymes. To date, Fe_3O_4 nanoparticles are the most well-recognized nanomaterials with enzyme-mimicking activity.^[18] Preparation of Fe_3O_4 nanoparticles inside the hollow cavity of FTn (Fe_3O_4 Fenozyme) under the same synthesis condition resulted in particles with similar sizes to MnO_2 Fenozymes, as assessed by TEM observation (**Figure S1c**, Supporting Information). Thus, in order to better understand enzyme-mimicking activities, Fe_3O_4 Fenozyme was used as control nanozymes in this study. It is well known that SOD catalyzes $\text{O}_2^{\cdot-}$ to generate H_2O_2 and that CAT decomposes H_2O_2 into nontoxic O_2 and H_2O , under physiological conditions. Therefore, SOD- and CAT-like activities of MnO_2 - and Fe_3O_4 -Fenozymes were evaluated in pH 7.4 buffer. The SOD activities of MnO_2 - and Fe_3O_4 -Fenozymes were compared (**Figure 1e**). The SOD-like activity of MnO_2 -Fenozymes was higher than Fe_3O_4 -Fenozymes in the same reaction condition. Furthermore, we investigated whether MnO_2 - and Fe_3O_4 -Fenozymes have CAT-like activity by measuring O_2 generation using a dissolved oxygen meter (**Figure 1f** and **Figure S1d**, Supporting Information). MnO_2 - and Fe_3O_4 -Fenozymes exhibited typical Michaelis–Menten kinetics—a model of enzymatic dynamics. The CAT-like activities of the MnO_2 Fenozyme were comparable with the Fe_3O_4 Fenozyme, as indicated by the values for K_m (Michaelis constant, the substrate concentration at which the initial rate is half of the maximum velocity) and k_{cat} (turnover number, the catalytic constant for the conversion of substrate to product), two parameters of enzyme catalytic efficiency (**Table S1**, Supporting Information). Furthermore, the $\text{O}_2^{\cdot-}$ scavenging ability of the Fenozymes was further studied by monitoring the fluorescent intensity of dihydroethidium (DHE), which is an $\text{O}_2^{\cdot-}$ specific indicator. The generation of $\text{O}_2^{\cdot-}$ was induced by xanthine oxidase as described,^[19] and subsequently the reduction of $\text{O}_2^{\cdot-}$ was evaluated by adding different concentrations of Fenozyme (**Figure 1g**). The results showed the gradual elevation of $\text{O}_2^{\cdot-}$ elimination rate as the concentration of Fenozyme increased, and $\text{O}_2^{\cdot-}$ eliminating abilities of MnO_2 Fenozymes were obviously better than Fe_3O_4 Fenozymes.

Next, POD activity—the catalysis of H_2O_2 to generate free cytotoxic radicals (such as OH^\cdot) under acidic conditions—was tested by colorimetric reaction when incubated with tetramethylbenzidine (TMB) substrates. Interestingly, we found the POD-like activity of the MnO_2 Fenozyme was low in the presence of TMB buffer (pH 4.5); in contrast, Fe_3O_4 Fenozyme showed a high POD-like activity (**Figure 1h**). Michaelis–Menten kinetics of the k_{cat} of Fe_3O_4 Fenozyme was >10 -fold higher than that of the MnO_2 Fenozyme (**Table S2**, Supporting Information). Using hydroxyphenyl fluorescein (HPF) as an OH^\cdot specific indicator, we also demonstrated that the OH^\cdot generation ability of the MnO_2 Fenozyme was markedly lower than that of the Fe_3O_4 Fenozyme (**Figure 1i**). Furthermore, we confirmed TPP modification did not obviously change POD-like activity (**Figure S1e**, Supporting Information) and OH^\cdot generation ability (**Figure S1f**, Supporting Information) of Fenozyme. Together, these results implied that the MnO_2 Fenozymes were capable of converting $\text{O}_2^{\cdot-}$ into nontoxic molecules through

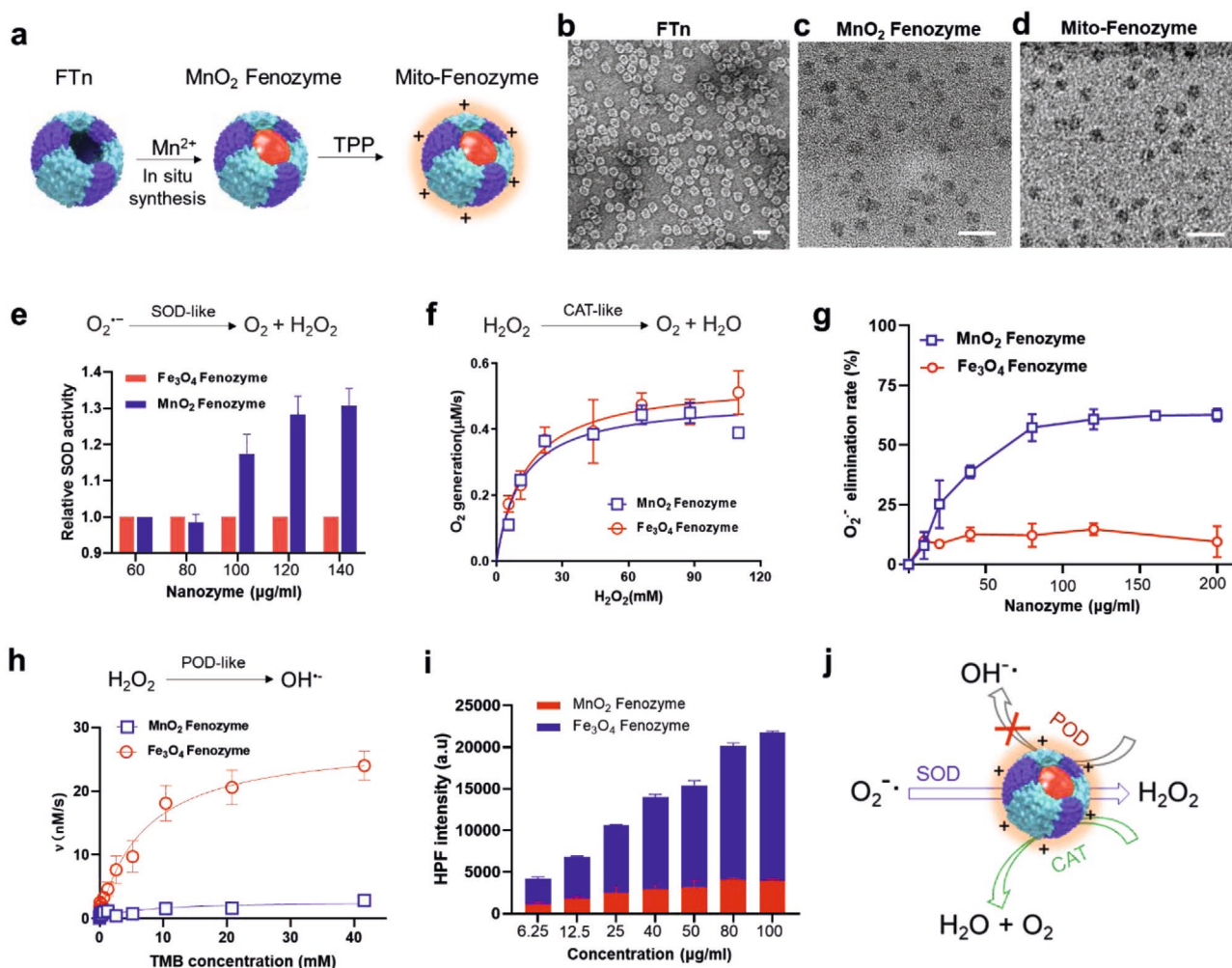


Figure 1. Preparation, characterization, and enzyme mimics of Fenozyme. a) Schematic illustration of preparation of Mito-Fenozyme. Mito-Fenozyme were fabricated by in situ synthesis of MnO₂ into FTn core via Mn²⁺ oxidation in the presence of H₂O₂, followed by TPP-NHS ester conjugation with free -NH₂ of protein. b–d) TEM images of FTn protein shell (negative staining with 1% uranyl acetate) (b), MnO₂ nanoparticles inside an FTn shell (c), and Mito-Fenozyme (d). Scale bar = 20 nm. e) The relative SOD-like activity of MnO₂- and Fe₃O₄-Fenozyme in the same condition. The activity of Fe₃O₄-Fenozyme was normalized to 1. f) Kinetics for CAT-like activity of MnO₂- and Fe₃O₄-Fenozyme. g) The O₂^{•-} scavenging capacity of MnO₂- and Fe₃O₄-Fenozyme using DHE as indicator. h) Kinetics for POD-like activity of MnO₂- and Fe₃O₄-Fenozyme in the same condition. i) Comparison of OH⁻ generation of MnO₂ Fenozyme and Fe₃O₄ Fenozyme in the same condition by using HPF probe as an indicator. j) Schematic illustration showed that created MnO₂ Fenozyme converted O₂^{•-} into nontoxic H₂O and O₂ by mimicking the cascade reaction of different enzymes (i.e., SOD and CAT) while not generating highly toxic OH⁻.

catalyzed cascade reactions of SOD and CAT but efficiently avoided H₂O₂ decomposition into highly cytotoxic OH⁻ as a result of low POD-like activity (Figure 1j).

The subcellular location of the nanozymes is a key factor for determining what kind of enzyme activity and scavenging efficiency of free radicals will occur. Mitochondria are the primary organelles for generation of O₂^{•-} and a primary origin for induced oxidative damage to cells.^[20] Our previous study demonstrated that FTn were trafficked into endo/lysosomes after cell uptake via interaction with its receptor,^[21] and thus, lysosomes are a determinant barrier against efficient mitochondrial targeting of FTn within the intracellular space. As such, we sought to explore whether TPP modification improved lysosomal escape and could induce mitochondrial accumulation of MnO₂ Fenozymes (Figure 2a, scheme). H9C2 cardiomyocytes

were incubated with Cy5-labeled Fenozyme-TPP (Mito-Fenozyme), and lysosomes were stained with LysoTracker. Confocal images showed that the MnO₂ Fenozyme primarily colocalized with lysosomes 2 h after addition to cells, whereas most of Mito-Fenozyme escaped from lysosomes (Figure 2a, middle). The quantification analysis of the colocalization of the particles and lysosomes demonstrated that the Pearson's coefficient of Mito-Fenozyme was ≈2.4-fold lower than the MnO₂ Fenozymes. We further studied whether Mito-Fenozymes actively accumulated into mitochondria after lysosomal escape (Figure 2b, scheme). Following costaining of mitochondria with Mitotracker, we found Mito-Fenozymes showed preferential mitochondrial accumulation (Figure 2b, middle). Quantification analysis indicated that the Pearson's coefficient of mitochondria colocalization with the MnO₂ Fenozymes and the

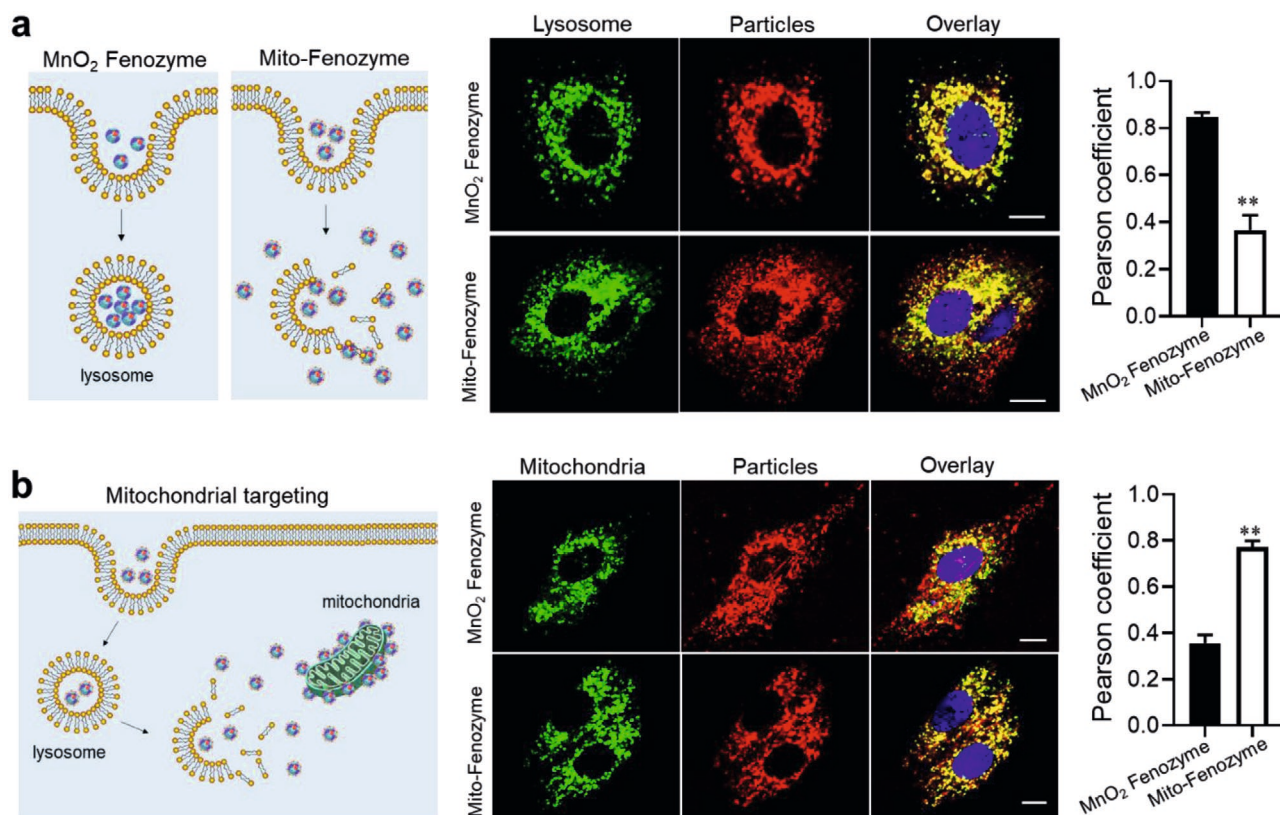


Figure 2. Mitochondrial accumulation of Mito-Fenozyme after lysosomal escape. a) Schemes of intracellular distribution of the particles after uptake (left); representative confocal images (middle) and quantification analysis (right) of the colocalization of the particles with lysosome stained with commercial LysoTracker. Scale bar = 10 μ m. b) Schematic illustration of intracellular fate of Mito-Fenozyme (left); typical confocal images (middle) and quantification analysis (right) of the colocalization of the particles with mitochondria stained with MitoTracker. Scale bar = 10 μ m. ** $P < 0.01$.

Mito-Fenozymes was 0.36 ± 0.07 and 0.77 ± 0.08 , respectively. The results demonstrated that the Mito-Fenozyme were capable of targeting mitochondria by overcoming the cell membrane and lysosomal barriers.

We next sought to investigate intracellular functions of the nanozymes on cardiomyocytes under oxidative stress conditions. We hypothesized that at least three aspects needed to be considered for the protective effect of the nanozymes after mitochondrial induced oxidative damage (Figure 3a): i) the scavenging ability of $O_2^{\cdot-}$ in the mitochondria; ii) the ROS level in the whole cells; iii) the protection effects of mitochondrial functions. First, the oxidative injury of H9C2 cells was induced through abrupt changes of oxygen levels following the established procedures, as previously reported.^[22] After staining with mitoSOX, a mitochondrial $O_2^{\cdot-}$ indicator, we observed that strong fluorescence signal was localized in mitochondria (Figure 3b, top left), whereas the signal intensity was decreased after MnO₂ Fenozyme and Mito-Fenozyme treatments. Further quantification analysis demonstrated nearly 68% and 33% reduction of mitochondrial $O_2^{\cdot-}$ when treated with Mito-Fenozyme and MnO₂ Fenozyme, respectively, compared to the cells with no Fenozyme treatment. Next, the generation and elimination of intracellular free radicals were investigated by flow cytometry analysis of the H9C2 stained with HPF. The results showed that activated HPF signal in cells treated with Fe₃O₄ Fenozyme was significantly higher than that of cells

treated with MnO₂ Fenozyme (Figure S2a, Supporting Information), and $OH^{\cdot-}$ production in cells treated with MnO₂ Fenozyme was negligible (Figure S2b, Supporting Information), which implied that the POD activity of MnO₂ Fenozyme in cells was also low. We then revealed the efficient elimination capacity of Mito-Fenozyme in the H9C2 subjected to oxidative damage by using 2',7'-dichlorodihydrofluorescein diacetate (DCFH) as an indicator of ROS free radicals (such as $OH^{\cdot-}$, $ONOO^-$, H_2O_2 , $O_2^{\cdot-}$) and observation by confocal microscopy (Figure 3c) and flow cytometry analysis (Figure 3d). Finally, we found Mito-Fenozyme significantly alleviated adenosine triphosphate (ATP) reduction of the oxidative damaged cells ($P < 0.05$), as evidenced by measuring the cellular ATP in untreated and treated cells (Figure 3e). Further RT-PCR analysis of mitochondrial DNA (mtDNA) copy number, an index of mitochondrial genomes per cell, was performed to evaluate mitochondrial function. The increased protective effect of Mito-Fenozyme on mtDNA was better than MnO₂ Fenozyme (Figure 3f). The results implied that Mito-Fenozyme eliminated mitochondrial $O_2^{\cdot-}$ and avoided the production of intracellular free radicals, providing efficient protection of mitochondrial functions in cardiomyocytes undergoing oxidative stress.

We sought to understand whether Mito-Fenozyme could target/accumulate within IR injured cardiac tissue after i.v. injection. Before this, we first evaluated TIM-2 expression, a receptor for FTh in mouse, in isolated cardiac IR tissues. IR

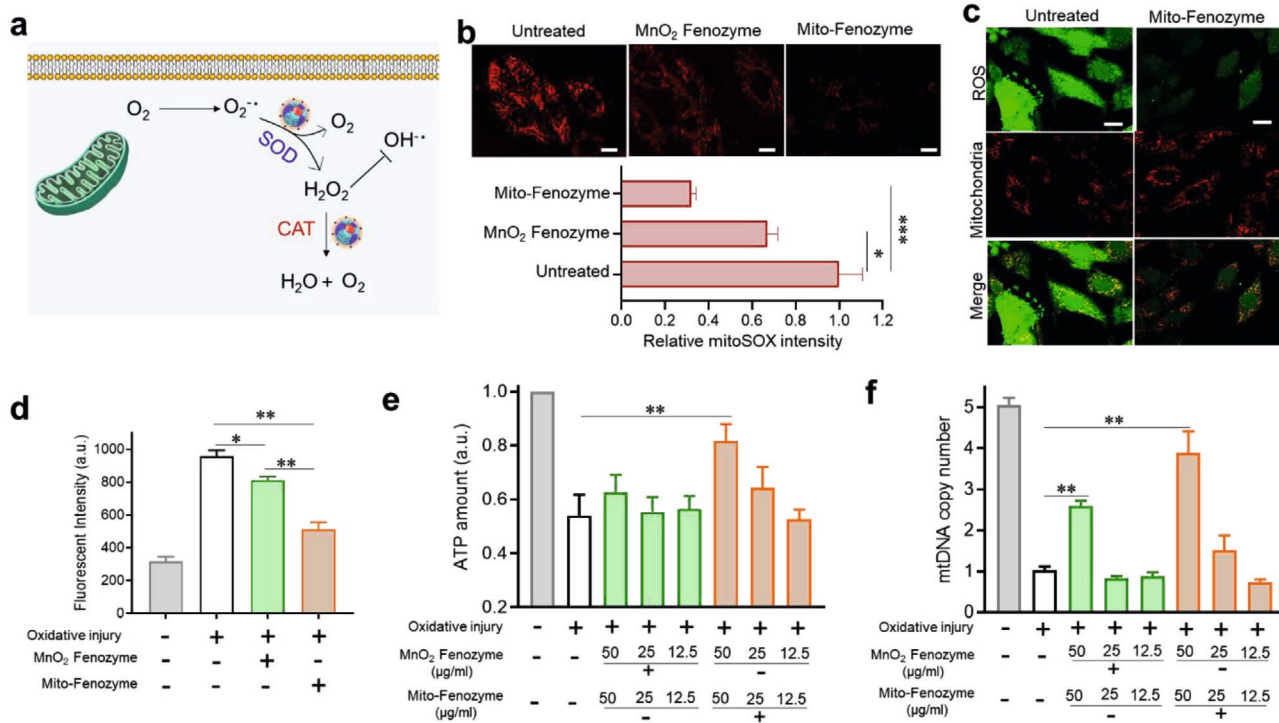


Figure 3. Intracellular protective effect of Mito-Fenozyme on H9C2 mitochondrial function via O₂^{-•} scavenging. a) Schematic illustration of intracellular conversion of free radicals to noncytotoxic molecules under Mito-Fenozyme. b) Confocal images (upper) and quantification analysis (bottom) of the effect of MnO₂ Fenozyme and Mito-Fenozyme on mitochondrial oxidative injury by mitoSOX as O₂^{-•} indicator. Scale bar = 10 µm. c) Representative images of intracellular free radical level in oxidative damaged H9C2 untreated and treated with Mito-Fenozyme using DCFH probe as a ROS indicator. Scale bar = 10 µm. d) Flow cytometry analysis of ROS level in H9C2 suffered from oxidative injury after different treatments. e) Effect of MnO₂ Fenozyme and Mito-Fenozyme on intracellular ATP amount in H9C2 subjected to oxidative injury. f) RT-PCR analysis of mtDNA copy number in cells following different treatments. **P* < 0.05, ***P* < 0.01, ****P* < 0.001.

injury was induced by blood reperfusion following ligation of the left anterior descending coronary artery. Western blot analysis showed obvious increased expression of TIM-2 in cardiac tissues subjected to IR surgery at 6 and 24 h, compared to sham animals (without IR surgery) (Figure 4a). The biodistribution of TPP-labeled FTn (FTn-TPP) was further evaluated by ex vivo fluorescence imaging. Tail-vein injection of the Cy5-FTn-TPP particles resulted in particles that were mainly distributed within the liver and kidney, regardless of sham and IR conditions (Figure S3, Supporting Information). At 1 h, we observed a slight increased signal from the particles that had remained within the IR heart, compared to the sham heart (Figure 4b). The elevated signal intensity of IR heart was further enhanced 24 h after injection, with nearly threefold higher than sham heart (*P* < 0.01). Subsequently, the hearts at 24 h were isolated, and the cryosection was observed by confocal microscopy. Histology images showed obvious accumulated distribution of injected particles in the frozen tissues isolated from the cardiac IR region (arrow) (Figure 4c, left). Quantification analysis revealed a significant increase of the mean signal intensity in the IR hearts compared to that of sham (*P* < 0.01) (Figure 4c, top right). We also determined the distribution of the particles in different region from the same IR hearts. Compared to the healthy region in IR hearts, there was about 12-fold enhancement of the particles in ischemic region (arrow) (Figure 4c, bottom right). Acute ischemia-initiated diseases tend to induce

physiological adaptive changes of injury tissues, especially in instances of hypoxic tissue microenvironments and increased vessel permeability.^[23] Our previous studies demonstrated FTn as a promising nanocarrier capable of actively binding with hypoxic cells to provide efficient tissue penetration, predominantly through interactions with its receptor (TfR-1 in humans; TIM-2 in mice).^[24] In addition to active targeting of FTn, we previously demonstrated that increased vessel permeability contributed to the improved nanoparticle accumulation in ischemic tissue,^[25] revealing the targeting ability of FTn to be dependent on both active and passive mechanisms.

To test the therapeutic potency of Mito-Fenozyme, the IR mice were administrated three doses of saline, MnO₂ Fenozyme, or Mito-Fenozyme via tail vein injection every 2 d. Echocardiography was performed 14 d after surgery, and the images indicated left ventricular wall motion in sham mice and IR mice after the different treatments, showing a varying extent of contraction functional damage in anterior/posterior walls (Figure 4d). Quantification analysis revealed that the parameters of left ventricular ejection fraction (LVEF, for cardiac function) and left ventricular fractional shortening (LVFS, for cardiac contractility) for the mice treated with saline had reduced to ≈50% of the sham mice, as expected (Figure 4e,f). In comparison to saline group, there was gradual improvement in the recovery of cardiac functionality when the mice were administered MnO₂ Fenozyme or Mito-Fenozyme, as evidenced

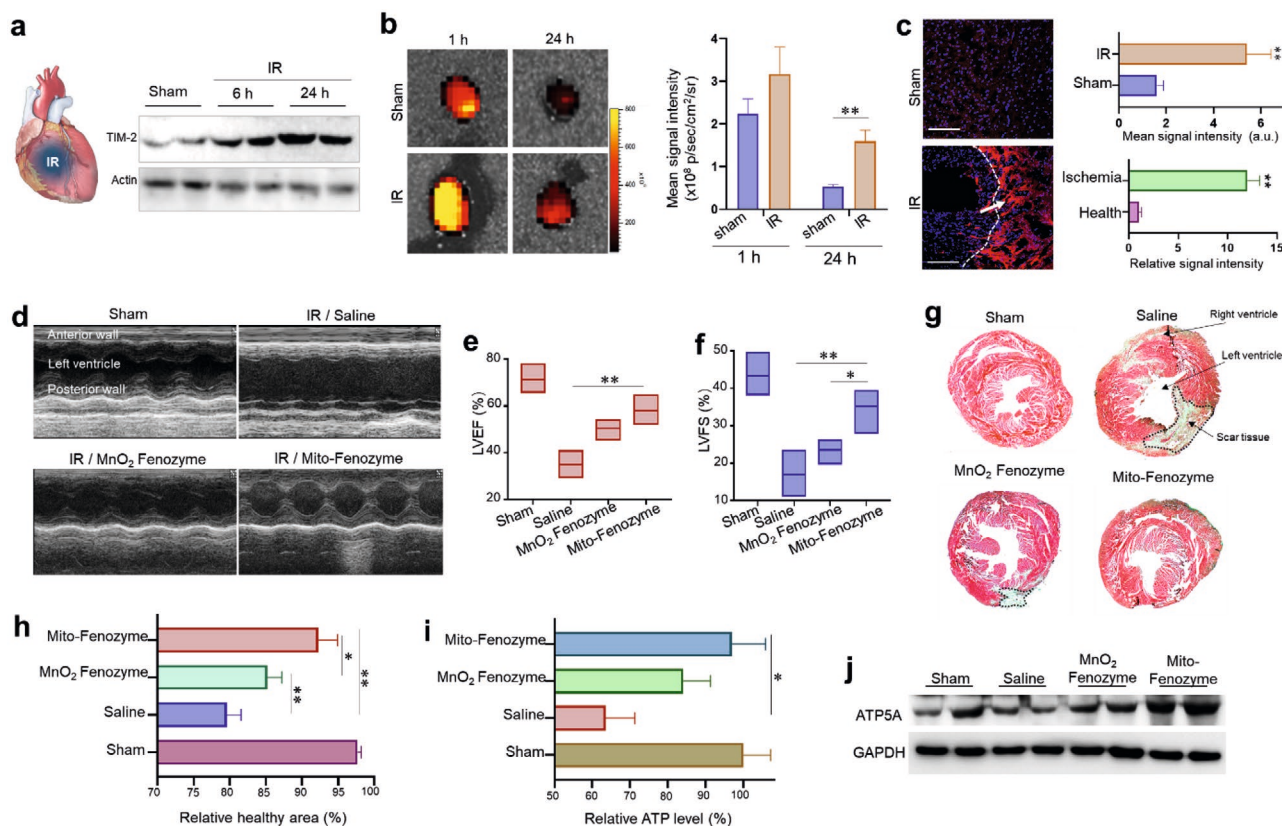


Figure 4. Accumulation and cardiac repair of Mito-Fenzoyme in a mouse IR model following i.v. administration. a) Western blot analysis of TIM-2 (i.e., FTn receptor) expression in sham and IR hearts isolated. b) Representative ex vivo fluorescence imaging of mouse hearts and quantification analysis of fluorescence intensities at different time points after tail vein injection of Mito-Fenzoyme into sham and IR mice ($n = 3$ per group). c) Representative images of distribution of Mito-Fenzoyme in sham and IR cardiac tissues of the mice 24 h after injection ($n = 3$ per group, at least ten slices each mouse). Scale bar = 100 μm . d) Echocardiographic images of the left ventricular wall motion of mice with or without treatments following IR surgery at 14 d ($n = 6-7$ per group). Quantification analysis of cardiac function of (d) left ventricular ejection fractions (LVEFs) and (e) left ventricular fractional shortening (LVFS). g) Representative images of midpapillary regions of the hearts, 14 d after IR using Masson's trichrome staining (blue, collagen-rich scar tissue; red, viable myocardium). The scar tissue was indicated with dashed box. h) Quantification analysis of healthy/scar area of the sham and IR hearts with or without treatments ($n = 6-7$ per group). i) Quantification analysis of mitochondrial functional parameter, ATP amount, in sham and IR cardiac tissues following different treatments ($n = 4-5$ per group). j) Western blot analysis of ATP5A expression in different heart tissues isolated from the mice without or with treatments. $*P < 0.05$, $**P < 0.01$.

by improved parameters of LVEF and LVFS. Next, mice were euthanized, and hearts were isolated for further evaluation by histological analysis. Figure 4g displayed the distribution of scar (blue) and healthy myocardium (red) tissue in hearts after Masson's trichrome staining, a standard method to assess tissue fibrosis. We observed that, in all mice subjected to IR surgery, the left ventricular walls were damaged as evidenced by the scar tissue, especially in the saline group. Quantification analysis revealed that more than 20% area of the whole heart was damaged for the mice treated with saline, whereas MnO₂ Fenozyme and Mito-Fenzoyme treatments efficiently decreased scar tissue accumulation ($P < 0.01$) (Figure 4h). Compared to the MnO₂ Fenozyme-treated group, the healthy area of the IR hearts was significantly improved after treatment with Mito-Fenzoyme ($P < 0.05$). Moreover, quantification analysis of ATP within sham and IR cardiac tissues demonstrated a significantly elevated mitochondrial functional recovery was found following Mito-Fenzoyme treatment, compared to the hearts from the saline group (Figure 4i). Western blot analysis further indicated that there was attenuated protein expression of mitochondrial

complex V subunit (ATP5A) after IR injury, but no reduction of ATP5A expression level was observed in Mito-Fenzoyme treated mice (Figure 4j). These results not only suggested that Mito-Fenzoyme effectively alleviated mitochondrial oxidative injury and improved functional recovery of cardiac tissues in mouse models after cardiac IR injury but also revealed the importance of mitochondrial targeting in oxidative injury. To understand whether there was systemic toxicity following i.v. administration, histopathological analysis was also performed by H&E staining on slices of tissues from major organs, 14 d after IR. The results suggested that there was no obvious accumulation of toxicities or signs of damage to the organs evaluated (Figure S4, Supporting Information).

Recently, tissue adhesive hydrogel-based cardiac patches have enabled the strong interface between biomaterials and epicardial tissue, aiding in the localized and controlled release of bioactive factors to help overcome tissue comorbidity and low retention resulting from direct tissue injection. Cardiac patches have demonstrated promising therapeutic potentials in various cardiac diseases.^[26] We thus sought to test whether

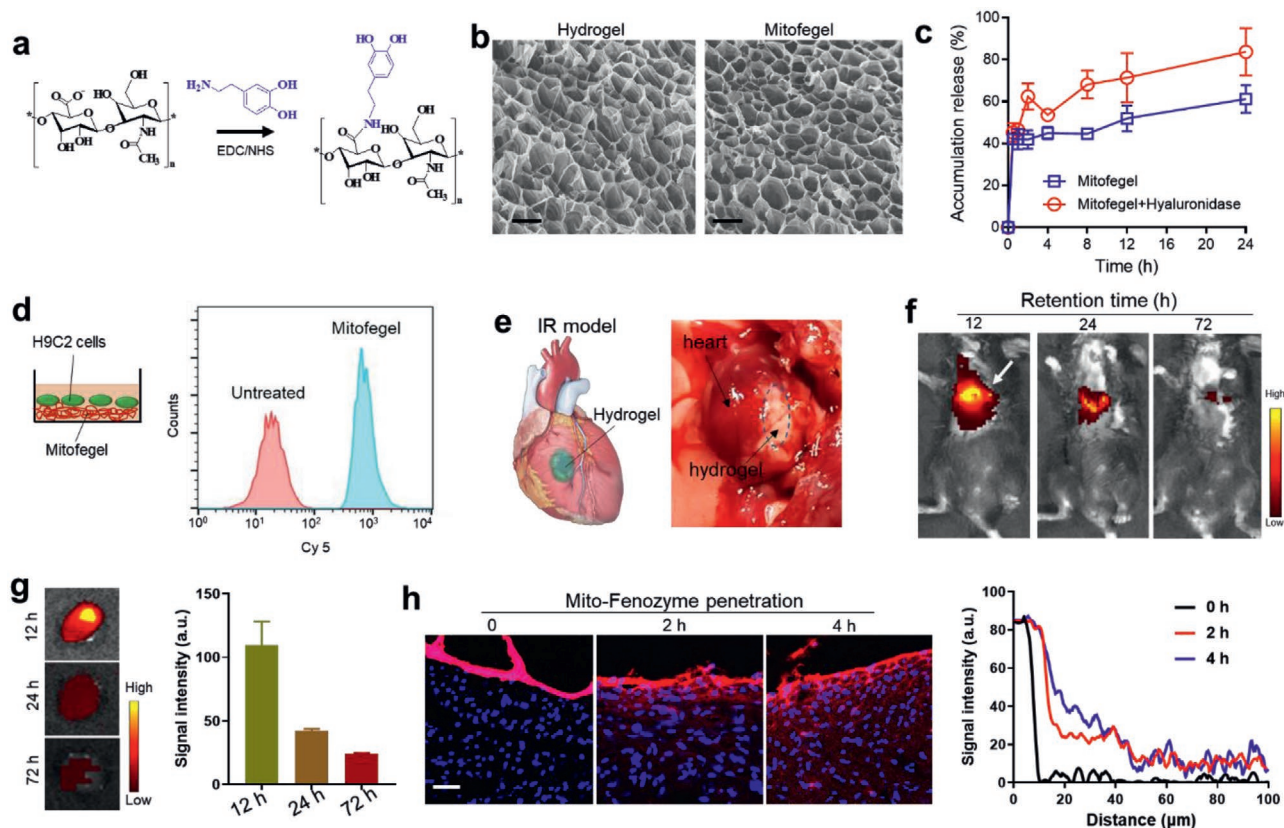


Figure 5. Preparation and properties of Mito-Fenozyme embedded into tissue adhesive hydrogel-based cardiac patch. a) Schematic illustration of CA conjugated with HA backbone (HA-CA) for the preparation of tissue adhesive hydrogel. b) Scanning electron microscopy imaging of the micropore structure of hydrogel and Mitofegel. Scale bar = 10 μm . c) Mito-Fenozyme release kinetics of Mitofegel in the presence and absence of hyaluronidase. d) The uptake of H9C2 following the cells plated onto solidified Mitofegel containing Cy5-labeled Mito-Fenozyme. e) The adhesion effect of HA-CA hydrogel on cardiac tissue in a mouse heart IR model. f) The retention capacity of cardiac patch containing Cy5-labeled Mito-Fenozyme on IR hearts over time ($n = 3$ per group). g) Representative fluorescence imaging of isolated hearts adhered with hydrogel at different time points (left), and quantification analysis of fluorescence intensities in isolated hearts (right) ($n = 3$). h) Distribution of Cy 5-labeled Mito-Fenozyme fluorescence signal in the isolated hearts. (Left) Representative images of penetration distance of Mito-Fenozyme following sticking on the hearts at different time points. Scale bar = 100 μm . (Right) Image-based quantification analysis of the mean intensity at different penetration distance ($n = 3$, at least eight slices for each mouse).

Mito-Fenozyme was able to provide therapeutic action through its combination with tissue adhesive hydrogels (Mitofegel). A biomimetic tissue adhesive hydrogel was prepared by conjugation of an adhesive catecholamine motif (CA) of mussel foot protein to the hyaluronic acid (HA) polymer backbone via carbodiimide coupling reactions (Figure 5a). The successful conjugation of HA and catecholamine motifs (HA-CA) was confirmed by nuclear magnetic resonance (NMR) and UV absorption spectrum (Figure S5a,b, Supporting Information). The rheological and viscoelastic properties revealed the hydrogel exhibited solid-like behavior after gelation, as determined by measuring the different hydrogel concentration for storage modulus (G') and loss modulus (G''), using dynamic mechanical analysis (Figure S5c, Supporting Information). Scanning electron microscopy (SEM) images showed interconnected microporous structure of the HA-CA hydrogel and the Mitofegel (Figure 5b). The pore size of the HA-CA hydrogel was mainly distributed between 5 and 10 μm , which was not significantly altered after loading of Mito-Fenozyme. We then tested the release kinetics of Mito-Fenozyme from the Mitofegel. A

burst release of Mito-Fenozyme was observed regardless of the presence and absence of hyaluronidase, reaching a maximum release of $\approx 40\%$ after 0.5 h (Figure 5c). However, the release of Mito-Fenozyme was obviously increased over time, and there was $>22\%$ elevation of the release percentage for the hydrogel treated with hyaluronidase at 24 h compared to that of the hydrogel alone.

We next tested whether Mito-Fenozyme was released and subsequently taken up by cardiomyocytes cultured on the hydrogels. The Mitofegel containing Cy5-labeled Mito-Fenozyme was solidified on the bottom of culture dishes and H9C2 cells were subsequently seeded onto the hydrogels (Figure 5d). Flow cytometry analysis displayed obvious signal changes within cells that had been cultured on hydrogels for 12 h, compared to the cells cultured on HA-CA hydrogels without Mito-Fenozyme. For the adhesive cardiac patch (i.e., the Mitofegel), the long-time adhesion on heart tissue and the deep penetration of Mito-Fenozyme into the myocardium are critical factors determining successful treatment of cardiac IR injury. As such, we first explored the in vivo retention ability

of the Mitofegel over time after adherence to hearts subjected to IR surgery. The images in Figure 5e,f show that Cy5-labeled Mito-Fenozyme embedding within hydrogels remained in the hearts and showed a gradual decrease in signal intensity over time, but could still be detected at 72 h postadhesion. Ex vivo imaging of isolated hearts also confirmed these results. Quantification analysis of the signal intensity of the hearts demonstrated that $\approx 38\%$ and 22% particles were kept in the hearts at 48 and 72 h compared to that at 12 h, respectively (Figure 5g). Subsequently, the diffusion/penetration of Mito-Fenozyme was investigated by cryosection of isolated IR heart tissues. We observed the particles accumulated on the epicardium within the hydrogel and the occurrence of diffusion/penetration of the Cy5-labeled particles from cardiac surface to the interior of the myocardium over time (Figure 5h). Quantification analysis of the signal intensity of the particle distribution revealed that the Mito-Fenozyme diffused/penetrated more than $100\ \mu\text{m}$ into the myocardium after 2 h posthydrogel adhesion. The results suggested that the Mito-Fenozyme embedded in the hydrogel was able to penetrate deep into cardiac tissue and be taken up by cardiomyocytes following its release by diffusion from the microporous structure of the hydrogel and the degradation of HA backbone by hyaluronidase in the cardiac tissue.^[27]

We sought to investigate whether Mito-Fenozyme loaded into adhesive cardiac patches would convey a protective effect on the myocardium, following IR injury. First, an acute protective action was explored by collecting hearts 24 h after local

adhesive cardiac patch treatments. The cardiac tissue damage was assessed by determining the observed coloration of five pieces of tissues isolated from each heart using triphenyl tetrazolium chloride (TTC) and Evans Blue double staining, which are widely used as indicators of not-at-risk and area-at-risk (AAR) regions and the infarct size determined by blue, red, and white-stained areas, respectively (Figure 6a). Macroscopic images showed the obvious infarct areas within the heart tissues subjected to IR, especially prominent in untreated hearts. Quantification analysis of the infarct size in each slice demonstrated that the infarcted area following Mitofegel treatment was smaller than other groups, and there were $\approx 42\%$, 38% , and 20% decreases in infarct size compared to untreated-, hydrogel alone-, and MnO₂ Fenozyme embedding into hydrogel (Fegel) treatments, respectively (Figure 6b).

To further understand the long-term protective effects of Mitofegel on cardiac IR injury, five groups were analyzed by hydrogel attachment before reperfusion: Sham, IR/Saline, IR/Hydrogel, IR/Fegel, and IR/Mitofegel. Echocardiography data were collected at 14 d post-treatments to assess cardiac function. Figure 6c–e exhibited that IR surgery induced functional damage to the cardiac anterior/posterior walls, but the cardiac function (measured by LVEF) and cardiac contractility (measured by LVFS) were significantly improved after treatments with Fegel or Mitofegel compared to untreated hearts ($P < 0.01$). Masson's trichrome staining showed the distribution of healthy (red) and scar (blue) tissue in hearts (Figure 6f),

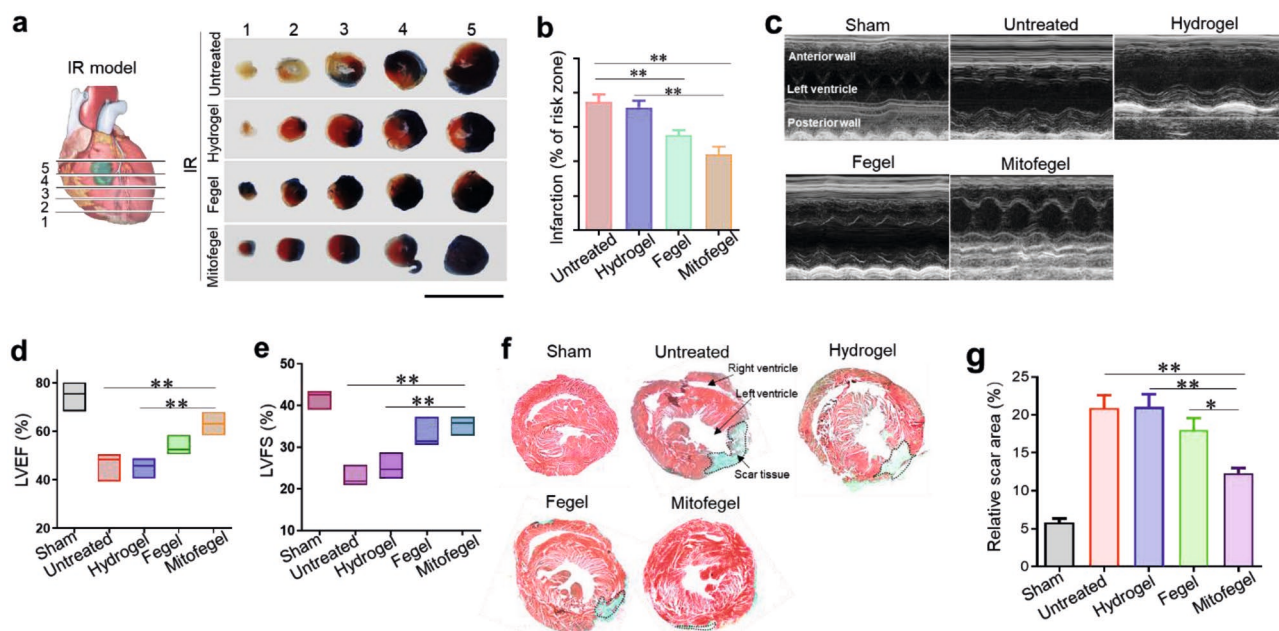


Figure 6. Effect of adhesive Mitofegel on mouse IR models and recovery of heart function. a) Heart sectioning for gross assessment of infarct size 24 h after IR surgery. (Left) Schematic showing five sections cut from apex to level of ligation. (Right) Representative images of five heart sections from one heart suffered from IR without or with different treatments ($n = 4$ per group), followed by Evans Blue and TTC double staining. The heart sections presented different regions determined by colors. Blue: nonischemic area; Red: area at risk; White: infarct size. Scale bar = 1 cm. b) Image-based quantification analysis of infarct size from (a) using ImageJ software. c) Representative echocardiographic images of the left ventricular wall motion of mice after hydrogel adhesion at 14 d ($n = 6$ per group). d,e) Quantification analysis of cardiac function of (c) by determining the parameters of left ventricular ejection fractions (LVEFs) (d) and left ventricular fractional shortening (LVFS) (e) ($n = 6$). f) Masson's trichrome staining of midpapillary regions of the hearts isolated. Blue: collagen-rich scar tissue; Red: viable myocardium. The scar tissue is indicated by the dashed box. g) Quantification analysis of scar area of (f) using ImageJ software ($n = 6$ per group). $*P < 0.05$, $**P < 0.01$.

revealing that Mitofegel treatment evidently and qualitatively reduced myocardial fibrosis at the microscopic level, compared to all other groups (Figure 6g). Moreover, immunostaining of isolated ischemic regions revealed significant alleviation of cardiac hypertrophy and obvious increases in capillary density following Mitofegel treatments, in comparison to other groups, as assessed by the standardized methodologies of wheat germ agglutinin- (Figure S6a,b, Supporting Information) and isolectin B4-staining (Figure S6c,d, Supporting Information), respectively.

In summary, we artificially created a biomimetic cascade nanozyme based on the hybridization of a recombinant protein scaffold modified for mitochondria-targeting and a Mn-based nanoparticle as the core of enzymatic activity. Unlike native Mn SOD, our artificial nanozyme also exhibited CAT-like characteristic enzyme activity. This hybrid nanozyme was capable of cascade conversion of $O_2^{\cdot-}$ into nontoxic O_2 and H_2O by intrinsically SOD-like and CAT-like activities but negligible $OH^{\cdot-}$ generation due to its low POD-like activity. In addition, the cascade nanozyme provided a highly efficient decomposition of ROS free radicals into nontoxic molecules. Our results revealed the advantages of the hybrid nanozyme in protecting against mitochondrial oxidative injury. Our artificial nanozyme was capable of i) overcoming the intracellular lysosomal barrier to escape into the cytoplasm and allowed for accumulation at mitochondria, ii) avoiding secondary damage resulting from highly cytotoxic $OH^{\cdot-}$ generation during $O_2^{\cdot-}$ elimination, iii) preferential accumulation and targeting to ischemic tissues after systemic delivery according to heightened expression of FTh receptor in ischemic tissues, and iv) rapid and deep penetration into cardiac tissues when locally administered in combination with adhesive hydrogel cardiac patches. Taking advantage of our tailored nanozymes, we addressed the demands of feasible systemic delivery for the targeted treatment of cardiac IR injury and local sustained treatment of cardiac IR injury. Our study showed that these benefits combined to provide effective therapy in animal models of cardiac IR injury, with outcomes that included alleviation of mitochondrial oxidative injury and the subsequent enhanced recovery of heart functionality.

Supporting Information

Supporting Information is available from the Wiley Online Library or from the author.

Acknowledgements

Y.Z. and A.K. contributed equally to this work. This work was supported by the National Natural Science Foundation of China (31870999, 82072054, 91959129, 81830060, 81921004, 81701839), the Natural Science Foundation of Tianjin (18JCYBJC40900), "the Fundamental Research Funds for the Central Universities," Nankai University (63191120, 63201102), Thousand Talents Program for Young Researchers, and Nankai University Hundred Young Academic Leaders Program. All animal studies were approved by the Animal Ethics Committee of Nankai University (Tianjin, China). The H9C2 cells were purchased from ATCC and cultured in Dulbecco's modified Eagle medium (Gibco) supplemented with 10% fetal bovine serum (BI, Biological Industries) and 1% penicillin–streptomycin.

Conflict of Interest

The authors declare no conflict of interest.

Keywords

de novo design, mitochondria, nanozymes, protein scaffolds, superoxide scavengers

Received: September 26, 2020

Revised: November 27, 2020

Published online: January 22, 2021

- [1] a) H. K. Eltzschig, T. Eckle, *Nat. Med.* **2011**, *17*, 1391; b) G. Heusch, *Nat. Rev. Cardiol.* **2020**, *17*, 773.
- [2] E. T. Chouchani, V. R. Pell, A. M. James, L. M. Work, K. Saeb-Parsy, C. Frezza, T. Krieg, M. P. Murphy, *Cell Metab.* **2016**, *23*, 254.
- [3] Y. Chen, M. B. Azad, S. B. Gibson, *Cell Death Differ.* **2009**, *16*, 1040.
- [4] a) P. Hart, M. Mao, A. de Abreu, K. Fricano, D. Ekoue, R. Minshall, A. Diamond, M. Bonini, *Nat. Commun.* **2015**, *6*, 6053; b) A. E. Dikalova, A. T. Bikineyeva, K. Budzyn, R. R. Nazarewicz, L. McCann, W. Lewis, D. G. Harrison, S. I. Dikalov, *Circ. Res.* **2010**, *107*, 106.
- [5] a) D. Salvemini, D. P. Riley, S. Cuzzocrea, *Nat. Rev. Drug Discovery* **2002**, *1*, 367; b) D. P. Riley, *Chem. Rev.* **1999**, *99*, 2573.
- [6] a) J. Wu, X. Wang, Q. Wang, Z. Lou, S. Li, Y. Zhu, L. Qin, H. Wei, *Chem. Soc. Rev.* **2019**, *48*, 1004; b) H. Wei, E. Wang, *Chem. Soc. Rev.* **2013**, *42*, 6060.
- [7] Y. Huang, J. Ren, X. Qu, *Chem. Rev.* **2019**, *119*, 4357.
- [8] a) B. Jiang, D. Duan, L. Gao, M. Zhou, K. Fan, Y. Tang, J. Xi, Y. Bi, Z. Tong, G. F. Gao, N. Xie, A. Tang, G. Nie, M. Liang, X. Yan, *Nat. Protoc.* **2018**, *13*, 1506; b) L. Gao, J. Zhuang, L. Nie, J. Zhang, Y. Zhang, N. Gu, T. Wang, J. Feng, D. Yang, S. Perrett, X. Yan, *Nat. Nanotechnol.* **2007**, *2*, 577; c) K. L. Fan, J. Q. Xi, L. Fan, P. X. Wang, C. H. Zhu, Y. Tang, X. D. Xu, M. M. Liang, B. Jiang, X. Y. Yan, L. Z. Gao, *Nat. Commun.* **2018**, *9*, 1440.
- [9] a) Y. Y. Huang, Z. Liu, C. Q. Liu, E. G. Ju, Y. Zhang, J. S. Ren, X. G. Qu, *Angew. Chem., Int. Ed.* **2016**, *55*, 6646; b) N. Singh, M. A. Savanur, S. Srivastava, P. D'Silva, G. Muges, *Angew. Chem., Int. Ed.* **2017**, *56*, 14267; c) N. Singh, S. K. Naveen Kumar, M. Geethika, G. Muges, *Angew. Chem., Int. Ed.* <https://doi.org/10.1002/anie.202011711>.
- [10] a) S. C. Lin, Y. Cheng, H. Zhang, X. Y. Wang, Y. Y. Zhang, Y. J. Zhang, L. Y. Miao, X. Z. Zhao, H. Wei, *Small* **2020**, *16*, 1902123; b) J. Yao, Y. Cheng, M. Zhou, S. Zhao, S. Lin, X. Wang, J. Wu, S. Li, H. Wei, *Chem. Sci.* **2018**, *9*, 2927.
- [11] M. T. Lin, M. F. Beal, *Nature* **2006**, *443*, 787.
- [12] F. Nastro, M. Chino, O. Maglio, A. Bhagi-Damodaran, Y. Lu, A. Lombardi, *Chem. Soc. Rev.* **2016**, *45*, 5020.
- [13] H. J. Kwon, M. Y. Cha, D. Kim, D. K. Kim, M. Soh, K. Shin, T. Hyeon, I. Mook-Jung, *ACS Nano* **2016**, *10*, 2860.
- [14] B. Chandramouli, C. Bernacchioni, D. Di Maio, P. Turano, G. Brancato, *J. Biol. Chem.* **2016**, *291*, 25617.
- [15] a) F. Bou-Abdallah, G. Zhao, G. Biasiotto, M. Poli, P. Arosio, N. D. Chasteen, *J. Am. Chem. Soc.* **2008**, *130*, 17801; b) M. Ardini, B. D. Howes, A. Fiorillo, E. Falvo, S. Sottini, D. Rovai, M. Lantieri, A. Ilari, D. Gatteschi, G. Spina, E. Chiancone, S. Stefanini, M. Fittipaldi, *J. Inorg. Biochem.* **2018**, *182*, 103.
- [16] F. L. Gao, J. Wu, H. Q. Gao, X. Y. Hu, L. H. Liu, A. C. Midgley, Q. Q. Liu, Z. Y. Sun, Y. J. Liu, D. Ding, Y. M. Wang, D. L. Kong, X. L. Huang, *Biomaterials* **2020**, *230*.
- [17] M. P. Murphy, R. A. Smith, *Annu. Rev. Pharmacol. Toxicol.* **2007**, *47*, 629.
- [18] Y. A. Zhang, Y. L. Jin, H. X. Cui, X. Y. Yan, K. L. Fan, *RSC Adv.* **2020**, *10*, 10.

- [19] S. Dikalov, T. Losik, J. L. Arbiser, *Biochem. Pharmacol.* **2008**, *76*, 589.
- [20] H. P. Indo, H. C. Yen, I. Nakanishi, K. Matsumoto, M. Tamura, Y. Nagano, H. Matsui, O. Gusev, R. Cornette, T. Okuda, Y. Minamiyama, H. Ichikawa, S. Suenaga, M. Oki, T. Sato, T. Ozawa, D. K. Clair, H. J. Majima, *J. Clin. Biochem. Nutr.* **2015**, *56*, 1.
- [21] X. L. Huang, J. Chisholm, J. Zhuang, Y. Y. Xiao, G. Duncan, X. Y. Chen, J. S. Suk, J. Hanes, *Proc. Natl. Acad. Sci. USA* **2017**, *114*, E6595.
- [22] Z. W. Sun, J. Han, W. T. Zhao, Y. Y. Zhang, S. A. Wang, L. F. Ye, T. T. Liu, L. R. Zheng, *Int. J. Mol. Sci.* **2014**, *15*, 18362.
- [23] N. F. Cerqueira, C. A. Hussni, W. B. Yoshida, *Acta Cir. Bras.* **2005**, *20*, 336.
- [24] X. Huang, J. Zhuang, S. W. Chung, B. Huang, G. Halpert, K. Negron, X. Sun, J. Yang, Y. Oh, P. M. Hwang, J. Hanes, J. S. Suk, *ACS Nano* **2019**, *13*, 236.
- [25] R. Zhang, W. Luo, Y. Zhang, D. Zhu, A. C. Midgley, H. Song, A. Khaliq, H. Zhang, J. Zhuang, D. Kong, X. Huang, *Sci. Adv.* **2020**, *6*, eaaz8011.
- [26] a) H. Yuk, C. E. Varela, C. S. Nabzdyk, X. Y. Mao, R. F. Padera, E. T. Roche, X. H. Zhao, *Nature* **2019**, *575*, 169; b) K. Huang, E. W. Ozpinar, T. Su, J. N. Tang, D. L. Shen, L. Qiao, S. Q. Hu, Z. H. Li, H. X. Liang, K. Mathews, V. Scharf, D. O. Freytes, K. Cheng, *Sci. Transl. Med.* **2020**, *12*, eaat9683.
- [27] K. S. Girish, K. Kemparaju, *Life Sci.* **2007**, *80*, 1921.